



**HAL**  
open science

## Validation of CFD simulations of the flow around a full-scale rowing blade with realistic kinematics

Yoann Robert, Alban Leroyer, Sophie Barre, Patrick Queutey, Michel Visonneau

### ► To cite this version:

Yoann Robert, Alban Leroyer, Sophie Barre, Patrick Queutey, Michel Visonneau. Validation of CFD simulations of the flow around a full-scale rowing blade with realistic kinematics. *Journal of Marine Science and Technology*, 2019, 24 (4), pp.1105-1118. 10.1007/s00773-018-0610-y . hal-02394848

**HAL Id: hal-02394848**

**<https://hal.science/hal-02394848>**

Submitted on 30 Sep 2020

**HAL** is a multi-disciplinary open access archive for the deposit and dissemination of scientific research documents, whether they are published or not. The documents may come from teaching and research institutions in France or abroad, or from public or private research centers.

L'archive ouverte pluridisciplinaire **HAL**, est destinée au dépôt et à la diffusion de documents scientifiques de niveau recherche, publiés ou non, émanant des établissements d'enseignement et de recherche français ou étrangers, des laboratoires publics ou privés.



Distributed under a Creative Commons Attribution 4.0 International License

# Validation of CFD simulations of the flow around a full-scale rowing blade with realistic kinematics

Yoann Robert<sup>1</sup> · Alban Leroyer<sup>1</sup>  · Sophie Barré<sup>1,2</sup> · Patrick Queutey<sup>1</sup> · Michel Visonneau<sup>1</sup>

## Abstract

This article deals with the validation of the modelling and numerical simulation of a rowing stroke, by means of CFD. Simplified but realistic strokes were performed in a towing tank with a rotating arm and a real flexible oar. Those laboratory conditions are better controlled than those of in situ trials. An FSI procedure is developed to take into account the oar bending, which is essential in the physics of this flow. The results show that this numerical framework is able to reproduce qualitatively the real flow including the breaking of the free surface around the blade and the transport of the air cavity behind it. The profiles of forces are well reproduced, with propulsive forces overestimated by 5–12% for their maxima. The study also focuses on the computation of the uncertainties. It is highlighted that, even for this well-controlled experimental equipment, the uncertainties on the quantities of interest are of about 11%. In other words, the experimental uncertainty covers the numerical errors. So, this numerical modelling is validated and can be used for design and optimisation of blades and oars, or to contribute to the better understanding of the boat–oar–rower system and its dynamics.

**Keywords** Computational fluid dynamics · Fluid–structure interaction · Rowing · Validation

## 1 Introduction

Over the last three decades, CFD simulations have been increasingly used in the industry and the academic research. This trend is explained by the ongoing development of the physical models and the numerical methods, allowing the results to be accurate enough to compete with experimental means such as wind tunnels and towing tanks. Together with these scientific advances, IT resources have been growing to the pace of Moore’s law, which has eased CFD usage. This tool has also been used intensively in sports engineering [4], especially in Formula One or sailing, where budgets allocated to the development are very high. In sports like rowing, where funding is less substantial, progress goes slower. However, some promising work has been produced.

For the non-specialist reader, the following definitions are given. A rowing stroke is a cycle composed of two parts: the

propulsion, where the oar blade is immersed, and the recovery, where it is in the air. The propulsion can also be divided into several phases: the catch, where the blade rapidly goes through the free surface (i.e. the air–water interface), the drive, where the rower transmits the power in a very short time, and the catch or finish, where the blade is removed from the water. We refer to a real rowing stroke when the cycle given above is respected and the elements of the following list of physically relevant considerations are at least taken into account: the blade kinematics is imposed by a human rower; it is modified due to the oar flexibility and the FSI; the free surface is well described; the dynamics of the boat–oars–rower system is well represented.

In rowing, the boat and the oar blades are crossing the free surface, and the flow around those two bodies are complex and atypical in naval hydrodynamics. The flow around the blade is particularly challenging to model. In fact, the blade is moving with six degrees of freedom (DOFs). During the catch, the blade breaks the free surface and possibly projects drops at the impact. Then, during the drive, a ventilation phenomenon appears, leading to some air trapped behind the blade and at its extremity. This air cavity follows the blade during almost all the rowing stroke. The oar bending is also a key element of the flow and must be handled

---

✉ Alban Leroyer  
alban.leroyer@ec-nantes.fr

<sup>1</sup> LHEEA Lab., UMR-CNRS 6598, Centrale Nantes, 1 rue de la Noë, 44321 Nantes, France

<sup>2</sup> CREPS des Pays de la Loire, Place Gabriel Trarieux, CS 21925, 44319 Nantes, France

with care. Indeed, the deflection modifies the incident angle defined as the angle between the oar axis and the direction of the velocity of the water relative to the blade. Another characteristic is the violent dynamics of the stroke, where the incident angle quickly varies.

The scope of the following state of the art is limited to the research works related to numerical simulations. However, it is not so restricted, since most of the quoted articles refer to experimental works chosen as configurations for the necessary step of validation of the numerical model, as the present article does.

The first reference showing the usage of CFD for the study of the flow around the blade dates back to 1993. Videv and Doi [22] performed simulations with a two-dimensional monofluid configuration. As the blade is fully immersed and the plane of study is horizontal, this results in a profile comparable to a hydrofoil. With this very simple approach, the authors conclude on the importance of capturing the very unsteady nature of the flow. Despite this highly important consideration, a lot of authors consider that the study of the flow can be done with a sequence of discrete stationary orientations of the oar. For instance, Coppel et al. [3] use the RANS solver *ANSYS Fluent* to run simulations essentially of stationary nature, without free surface, using the three-dimensional geometries of a flat blade and a Big Blade. The rotation of the blade is done with a cylindrical sliding mesh. As the configuration radically simplifies the physical problem, the numerical results for the drag and lift coefficients get far from the experimental ones of Caplan and Gardner [2]. Sliasis and Tullis [18] also replicate the same case using the same solver but taking account of the free surface and therefore obtain better results.

Kinoshita et al. [6] were the first ones to carry out three-dimensional unsteady computations for this flow. However, the configuration was simple and unrepresentative of a real rowing stroke since the blade rotates around a vertical axis passing at mid-chord, with a uniform flow velocity and without free surface. Sliasis and Tullis [19] also performed unsteady computations using *ANSYS CFX* and demonstrated that the maxima of unsteady forces are significantly higher than the steady ones. Yet the results are unphysical at some point, especially for the propulsive force which is momentarily and unexpectedly negative. This default was corrected in another paper published later [20]. Leroyer et al. [8] performed simulations reproducing a simplified rowing stroke but with a dynamic similar to a real one, especially for the free surface deformation. In this case, the oar is rigid and the blade is flat and at scale 0.7. The results are in good agreement with experimental values. The authors continue their analysis of the flow [9] and conclude that the free surface and the unsteadiness are of paramount importance but viscous contributions are negligible. They also set up a modelling of a real rowing stroke [10], also used by Robert

et al. [15]. The kinematics of the blade comes from in situ recordings, i.e. where an instrumented boat was used by an elite rower on a river. Those measurements serve as input data for the simulations. The oar flexibility is also taken into account, with linear and angular deflections proportional to the main bending moment. In this strong coupling—here for the first time in the rowing literature—the position and the orientation of the blade are updated at each non-linear iteration of the flow solver *ISIS-CFD*, in function of the hydrodynamic forces and moments acting on the blade. The obtained results show that the dynamic of the rowing stroke is well captured, despite a difference with the experimental results for the propulsive moment which grows quickly at a given angular interval and reaches up to 15-20%. This deviation might come from an inaccurate capture of physical phenomena (transport of the air cavity attached to the blade, flow separation, etc.). However, since such a default does not appear in the present results, it is more likely due to higher uncertainties on the measurements aboard the instrumented boat and because some DOFs are not measured.

The aim of the article is to show that the numerical modelling that we initiated [15] and improved is able to finely reproduce a realistic rowing stroke obtained in laboratory conditions, where uncertainties on measurements are smaller than in situ trials.

## 2 Methods

### 2.1 Experimental configuration

In 1999 an experimental campaign was carried out in the towing tank of the LHEEA Laboratory. The experimenters have designed accurate, controlled and repeatable test means to generate a simplified rowing stroke with a realistic kinematics. An arm allows the rotation of the oar and the carriage of the towing tank is used to produce a uniform translation (see Fig. 1). This configuration enables to decouple the study of the propulsive system (i.e. the oar blade) from the motor (i.e. the rower). Therefore one can observe, characterise and model the hydrodynamic forces and moments in function of several parameters.

The towing tank had a length of 70 m in 1999<sup>1</sup>, a width of 5m and a depth of 3m. The length is sufficient to perform a rowing stroke, considering the acceleration and deceleration phases of the carriage. Given the length of the oar, the axis of rotation is shifted from the midplane to increase spacing between the blade and the vertical wall. The blade chord is small enough relative to the water depth to neglect the vertical confinement.

<sup>1</sup> The towing tank has a length of 140 m today.

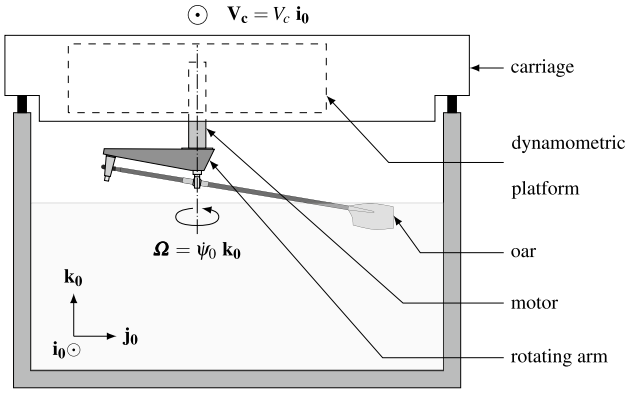


**Fig. 1** Sketch of the experimental configuration used to generate a simplified rowing stroke in a towing tank with a real oar blade (non-real dimensions)

A six-component dynamometric platform is used to measure all the forces and moments and is installed on the carriage. Strain gauges are located on the sensitive part of the platform. The internal forces and moments of the transmission are not taken into account. In this way the hydrodynamic, aerodynamic and inertial forces are measured. Specific tests are carried out with the oar in the air to model aerodynamic and inertial forces. Those force models are verified by comparing with a trial performed in the air using a kinematics identical to one of those chosen for the trials (oar in water). Using those models, the hydrodynamic forces are retrieved by subtracting the aerodynamic and inertial forces from the measured forces.

A rotating arm, whose frame is lightweight and made of a carbon-fibre composite material, was specifically designed for those trials. Like in the real case, the oar is linked to this device at two points: one at the handle location and the other one at the oarlock location. The oar orientation is defined using the Cardan angles with the configuration given in Fig. 2. Three successive rotations enables to define the oar orientation. The first rotation of an angle  $\psi_0$  called

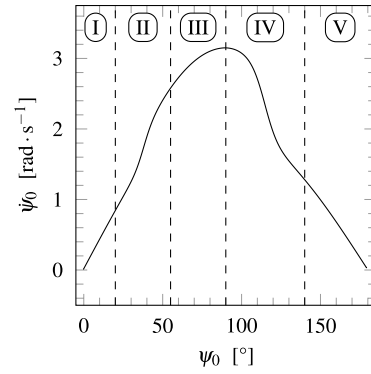


**Fig. 3** Angular velocity versus angular position of the oar for the simplified rowing stroke, splitted in five phases: (I) neutral kinematics; (II) catch-like phase; (III) phase at constant kinematic efficiency; (IV) finish-like phase; and (V) stop phase

sweep angle (classically called yaw angle) and around the vector  $\mathbf{k}_0$  changes the original basis  $(\mathbf{i}_0, \mathbf{j}_0, \mathbf{k}_0)$  to the basis  $(\mathbf{i}_1, \mathbf{j}_1, \mathbf{k}_1)$ , with  $\mathbf{k}_1 = \mathbf{k}_0$ . The second rotation of an angle  $\theta_1$  called immersion angle (classically called pitch angle) and around the vector  $\mathbf{j}_1$  changes the basis  $(\mathbf{i}_1, \mathbf{j}_1, \mathbf{k}_1)$  to the basis  $(\mathbf{i}_2, \mathbf{j}_2, \mathbf{k}_2)$ , with  $\mathbf{j}_2 = \mathbf{j}_1$ . Finally, the third rotation of an angle  $\phi_2$  called roll angle and around the vector  $\mathbf{i}_2$  changes the basis  $(\mathbf{i}_2, \mathbf{j}_2, \mathbf{k}_2)$  to the basis  $(\mathbf{i}_3, \mathbf{j}_3, \mathbf{k}_3)$ , with  $\mathbf{i}_3 = \mathbf{i}_2$ . The roll angle  $\phi_2$  and the immersion angle  $\theta_1$  are constant during the trial and the sweep angle  $\psi_0$  varies from about 0 to 180°.

The geared motor unit consists of a high-specific-power brushless motor. A digitally controlled drive imposes a 200-Hz-sampled speed command to the motor. An example of the laws imposed in the trials, composed of the five phases explained hereafter, is given in Fig. 3. As the carriage cannot be vertically moved during the test, the blade is immersed from the beginning to the end of the stroke. Furthermore, the trial cannot begin with the oar already oriented at the attack angle because it would cause unsuitable perturbations. So the phase I starts with the oar almost aligned to the carriage direction, at an angle earlier found that does not generate

**Fig. 2** Definition of the Cardan angles giving the orientation of the oar relative to the boat (or carriage). a Sweep angle  $\psi_0$ ; b Immersion angle  $\theta_1$ ; c Roll angle  $\phi_2$

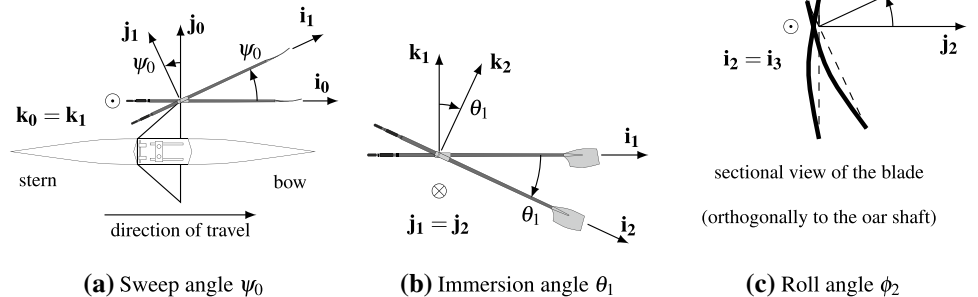


**Table 1** List of the experimental trials used and their parameters

# Trial	$V_c$ (m s <sup>-1</sup> )	$\phi_2^c$ (°)	$\theta_1$ (°)
59	4.0	0	10.5
61	4.0	4	10.5
63	4.0	10	10.5
67	4.0	8	11.5
99	4.1	4	11.5
109	4.1	4	9.5
122	4.1	4	10.5
154	4.2	6	9.5

any transversal force, and the angular velocity is such that the least possible flow perturbations are created. The phase II models the catch, corresponding to a rapid increase of the velocity at  $\psi_0 = 35^\circ$ . The phase III is performed at a constant kinematic efficiency  $\eta$  (detailed in the Sect. 4). The phase IV is a transition to the finish, in which the blade should get out of water in a real stroke and where the velocity rapidly decreases at  $\psi_0 = 120^\circ$ . The phase V is done at a moderate velocity to avoid needless stress on the structure and the sensors.

The fact that this rowing stroke is simplified is because the blade is always immersed and because the kinematics is not imposed as a human would do: it is not the same kinematics and the motor imposes the oar orientation regardless of the hydrodynamic forces applied on the blade (i.e. there is no dynamic feedback reaction, as a rower is naturally submitted to).

Different values of the immersion and roll angles are tested, as well as for the carriage velocity  $V_c$ . The list of the trials used in this article is presented in Table 1. The variable  $\phi_2^c$  corresponds to the opposite of  $\phi_2$ , to match the usual convention in rowing. The vertical reference is such that, when the oar is oriented with  $\phi_2 = 0^\circ$  and  $\theta_1 = 9.5^\circ$ , the top edge of the blade is awash.

A 12-bit Keithley DAS1602 computer board is used to record the signals of the three forces and three moments at a given point, the angular position and velocity, with a sampling rate of 500 Hz. As the recording is subject to noise of different natures coming from the experimental environment (e.g. the platform and rolling noise), a low-pass filtering with a cutoff frequency of 11 Hz is realised.

## 2.2 Numerical configuration

The fluid solver used is *ISIS-CFD*. It is developed by the METHRIC<sup>2</sup> group of the LHEEA Lab and available as

<sup>2</sup> The acronym METHRIC comes from the French for Modelling of High-Reynolds Incompressible Turbulent Flows and Couplings

a part of the *FINE<sup>TM</sup>/Marine* computing suite, which is dedicated to marine applications. This is an incompressible unsteady Reynolds-averaged Navier–Stokes (RANS) solver, based on a fully unstructured finite-volume method to build the spatial discretisation of the conservation equations. The pressure-velocity coupling is obtained through a Rhie & Chow SIMPLE-like method: at each time step, the velocity is updated from the momentum equations and the pressure is given by the law of mass conservation, transformed into a pressure equation. An arbitrary Lagrangian Eulerian (ALE) formulation is used to take into account the modification of the fluid spatial domain [8]. It is associated with robust and fast grid deformation techniques [11]. The temporal discretisation scheme is the backward difference formula of order 2 (BDF2) when dealing with unsteady configurations. For each time step, an inner loop, also called non-linear loop, associated to a Picard linearisation is used to solve the non-linearities of the system and to converge all the sequential coupled equations. Free-surface flows are addressed with interface-capturing methods, by solving a convection equation for the volume fraction of water, which is discretised with specific compressive discretisation schemes [13]. The code is fully parallel using the message passing interface (MPI) protocol. An automatic adaptive grid refinement technique [23] and a sliding grid method are also included.

The computational domain is a rectangular cuboid of dimensions 5m × 5m × 3m whose centre initially coincides with the blade root, i.e. the intersection of the shaft and the oar blade, as illustrated in Fig. 4a. This domain follows rigidly the body of the oar. It is large enough since the use of a larger domain has given identical results. This is explained by the fact that a rowing stroke takes place in a relatively confined space, as it can be seen in Fig. 6 or Fig. 2 of [15]. Indeed, the blade trajectory draws a flattened loop. The free surface location is by definition the  $z = 0$  m plane. All the meshes are created with the software *Hexpress<sup>TM</sup>*. As it can be seen in Fig. 4b, c, the mesh is refined vertically around the free surface and in a more isotropic manner inside a box surrounding the blade. To perform a grid convergence study three levels of mesh fineness are tested. The approximate numbers of cells for each grid are given in Table 2.

The rigid body motion is planar because the axis of rotation of the arm is perpendicular to the translation vector of the carriage. The reference point chosen for the rotation is the blade root. The temporal evolution of the sweep angle comes from the integration of the angular velocity given in Fig. 3. As the blade root is not located on the axis of rotation, it means that two translations have to be imposed to the blade: one colinear to  $\mathbf{i}_0$  and another one along  $\mathbf{j}_0$ . Before the stroke generation, a transient phase has to be added. It contains a 1-s acceleration of the carriage with an adjustment

**Fig. 4** Views of the computational domain and a  $1.2 \cdot 10^6$ -cell grid used for the numerical simulations of a simplified rowing stroke. **a** Computational domain. **b** Sectional view at  $X_0 = 0.3$  m. **c** Surface mesh of the Hatchet-kind blade (external face)

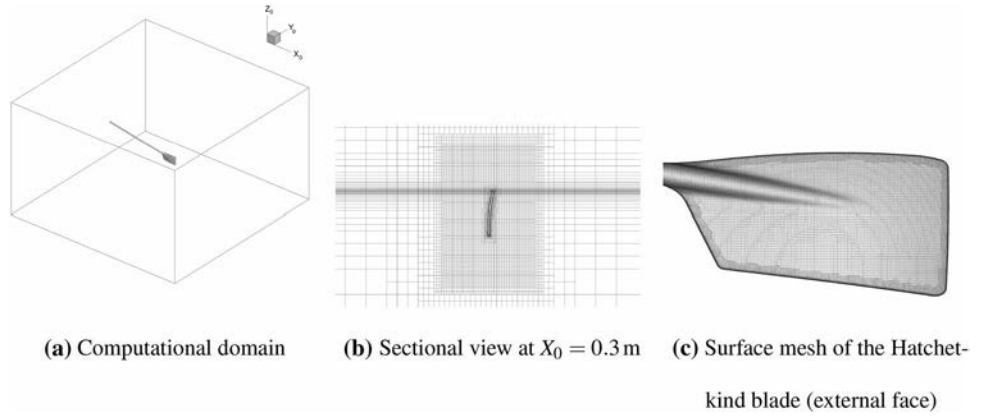


**Table 2** Number of cells (expressed in millions) of the grid used for the simulations

Grids		Coarse	Medium	Fine
Trials	67	1.2	2.7	12.3
	154	1.2	2.7	11.4
	Others	0.8–1.3	–	–

of the oar orientation<sup>3</sup> and it is followed by a 1.5-s phase to make the flow converge.

A Dirichlet condition is applied on the four vertical boundaries of the domain, where a null velocity is imposed (i.e. a far field condition). For the two faces at the top and the bottom, another kind of Dirichlet condition is used: the pressure is set to its atmospheric value. A wall function is applied on the blade and the shaft.

The temporal discretisation scheme is the backward differencing scheme of second order (BDF2) to deal with this unsteady configuration. To ensure the stability of the FSI coupling, the convergence of the non-linear loop is achieved when a reduction of 4 orders of the residuals is obtained or, by default, when 15 non-linear iterations are performed. The pressure is solved using the multigrid BoomerAMG solver [5], also with 4 orders, or 50 iterations to the maximum. For the simulation of a real rowing stroke, the use of a Euler model is sufficient because the viscous effect is negligible, as shown by Leroyer et al. in [9]. However, for the particular rowing stroke treated in this article, the viscous effect is not negligible anymore for the first and the last phases. Indeed, for the phases I ( $\psi_0$  close to  $0^\circ$ ) and V ( $\psi_0$  close to  $180^\circ$ ), the oar is approximately aligned with the direction of the carriage and sees a large magnitude of incident velocity. The  $k - \omega$  SST turbulence model of Menter [12] is then used.

<sup>3</sup> If the trial starts with an oar set to an angle  $\psi_0 = 0^\circ$ , it may generate large oscillations and disturb the flow. To avoid this behaviour, the oar is set to a slightly different angle, such that the lift force is null.

In addition to having a sufficiently fine mesh to capture the free surface around the blade, the Courant number also has to remain below 0.3 so that the interface-capturing BRICS scheme used for the resolution of the volume fraction keeps full compressivity properties. This constraint implies that the time step is limited and the CPU time increases consequently. A specific time-integration method [14, 16], which is called sub-cycling algorithm, was developed in order to speed up unsteady computations. It is based on the resolution of the convection equation for the volume fraction in several successive steps in which the associated time step (and thus the Courant number) is smaller. The other equations remain unchanged and are solved using a larger global time step. Since the resolution of the volume fraction has a very limited CPU cost, this technique enables to decrease the total computation time, without loss of accuracy. Validations were carried out on two- and three-dimensional test cases. It has led to the conclusion that, with this procedure, the CPU time is reduced by a factor usually between 3 and 4.

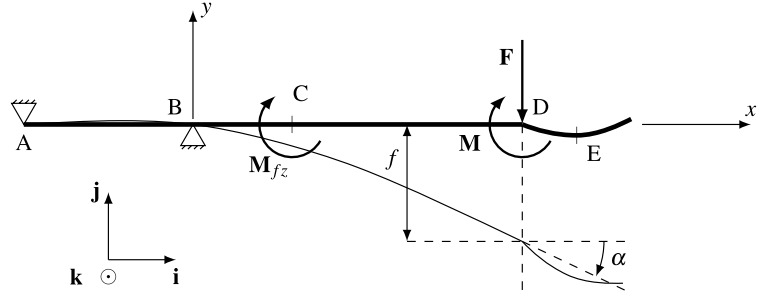
## 2.3 Structural model of the oar and FSI coupling

### 2.3.1 Structural model of the oar

The flexibility of the oar shaft is taken into account. Thus the imposed kinematics of the blade is modified and depends on the fluid loads which apply on this one, according to a law given hereafter. In return the flow is also altered, so are the hydrodynamic forces. The FSI coupling which has been developed can be qualified as strong. Indeed there is a convergence loop in the FSI coupling, coinciding with the resolution of the fluid solver. The variables are exchanged and updated at each non-linear iteration [11, 25].

The inertial effects of the oar are small compared to the fluid forces acting on the blade, that is why a resolution of the static equilibrium of the structure is suitable. The linear ( $f$ ) and angular ( $\alpha$ ) deflections are only considered in the  $(D, \mathbf{i}_3, \mathbf{j}_3)$  plane associated to the frame linked to the oar. Deflections outside this plane are far weaker therefore neglected. Two models

**Fig. 5** Modelling of the bending of the oar shaft



have been tested for the modelling of the oar bending, which is described in Fig. 5. The first one, denoted as *simplified model*, uses a proportionality between the bending moment at the sensors location (point C, merged with point B in this configuration) and the linear and angular deflections, as given by the system (1). The second model, designated by *complete model*, comes from laws of the beam theory and links directly the hydrodynamic force  $F$  and moment  $M$  (at the point D) to the deflections, as shown by the system (2). The oar is fixed to the rotating arm at two points A and B representing, respectively, the handle and the oarlock locations, separated by a distance  $L_i = 0.800$  m, also known as inner lever. The distance between the axis of rotation and the blade root (point D) along the oar axis is  $L_e = 1.558$  m. The point E is a rough approximation of the point where the hydrodynamic force is applied and it is located at a distance  $l = 0.258$  m of the point D. In fact it is mostly the point where loads were applied on a test bench for the determination of the coefficients  $K_{\text{lin}} = 3.4241 \cdot 10^3$  N and  $K_{\text{ang}} = 2.948 \cdot 10^3$  N · m.

$$\begin{cases} f = \frac{1}{K_{\text{lin}}} M_{fz}(C) \\ \alpha = \frac{1}{K_{\text{ang}}} M_{fz}(C) \end{cases} \quad (1)$$

$$\begin{cases} f = a M(D) + b F \\ \alpha = c M(D) + d F \end{cases} \quad (2)$$

The coefficients of the complete model depend on geometrical and mechanical parameters, according to equations (3)

$$\begin{aligned} a &= \frac{1}{(E I_{G_z})_{\text{lin}}} \left( \frac{L_e}{2} + \frac{L_i}{3} \right) L_e, \\ b &= \frac{1}{(E I_{G_z})_{\text{lin}}} (L_e + L_i) \frac{L_e^2}{3}, \\ c &= \frac{1}{(E I_{G_z})_{\text{ang}}} \left( L_e + \frac{L_i}{3} \right) \quad \text{and} \\ d &= \frac{1}{(E I_{G_z})_{\text{ang}}} \left( \frac{L_e}{2} + \frac{L_i}{3} \right) L_e, \end{aligned} \quad (3)$$

where  $E I_{G_z}$  is the product of the Young's modulus by the second moment of area along the  $z$  axis and at the point D. It is also called flexural rigidity and its value along the oar axis was studied by Laschowski et al. [7]. Different values are chosen for the linear or angular deflections for a better fitting:  $(E I_{G_z})_{\text{lin}} = 4.3872 \cdot 10^3$  N · m<sup>2</sup> and  $(E I_{G_z})_{\text{ang}} = 3.3778 \cdot 10^3$  N · m<sup>2</sup>.

### 2.3.2 FSI coupling

This FSI coupling cannot be used as is. Because of the added mass effect, a part of the fluid forces on the blade depends on the acceleration and may lead to the divergence of the numerical coupling [21]. To keep it stable, the position of the blade is updated at each non-linear iteration including a physical relaxation depending on an accurate computation of the added mass, whose procedure comes from Yvin et al. [24, 25] but adapted for the quasi-static approach used here. The computation of the  $6 \times 6$  added-mass matrix  $MA$  is done through the resolution of a Laplace operator to obtain the real added mass.

### 2.3.3 Stabilisation using the added mass for the FSI coupling with the simplified model

For the simplified model, defined by (1), we modify two DOFs of the blade,  $f$  and  $\alpha$ , but both are proportional. The stabilisation of one of them leads to the stabilisation of the other one. So, we can work only on the stabilisation of one DOF.

According to the principle of angular momentum on the blade, written at the sensor location (point C) and in the basis associated to the blade, we have the following relation:

$$I \ddot{\alpha} = M_z - K_{\text{lin}} f + M_{\text{in}}, \quad (4)$$

where  $I$  is the moment of inertia along the third axis of the basis,  $M_z$  the moment of the hydrodynamic forces at the point D along the same axis and  $M_{\text{in}}$  is the moment of inertia due to the non-Galilean nature of the considered frame. Furthermore, the fluid forces and moments are composed of two parts, as it appears in (5): the first one is independent of

the acceleration (written with the overline), the second one depends on it through the added-mass matrix  $MA$ .

$$\begin{pmatrix} F_x \\ F_y \\ F_z \\ M_x \\ M_y \\ M_z \end{pmatrix} = \begin{pmatrix} \overline{F_x} \\ \overline{F_y} \\ \overline{F_z} \\ \overline{M_x} \\ \overline{M_y} \\ \overline{M_z} \end{pmatrix} - \begin{pmatrix} MA_{11} & MA_{12} & MA_{13} & MA_{14} & MA_{15} & MA_{16} \\ MA_{21} & MA_{22} & MA_{23} & MA_{24} & MA_{25} & MA_{26} \\ MA_{31} & MA_{32} & MA_{33} & MA_{34} & MA_{35} & MA_{36} \\ MA_{41} & MA_{42} & MA_{43} & MA_{44} & MA_{45} & MA_{46} \\ MA_{51} & MA_{52} & MA_{53} & MA_{54} & MA_{55} & MA_{56} \\ MA_{61} & MA_{62} & MA_{63} & MA_{64} & MA_{65} & MA_{66} \end{pmatrix} \begin{pmatrix} \ddot{x} \\ \ddot{y} \\ \ddot{z} \\ \ddot{x} \\ \ddot{y} \\ \ddot{z} \end{pmatrix}, \quad (5)$$

Here we consider that the component dependent on the added mass mainly responds to  $\ddot{f}$ , which is here equal to  $\ddot{y}$ , i.e. the acceleration normal to the blade. In other words, all the terms of  $MA$  except  $MA_{22}$  are neglected. This hypothesis is linked to the model, based on a deformation of the oar due to an orthogonal force applied on the blade. Besides, the model is expressed using the moment  $M_z$ . So, we choose a value  $MA_{62} = MA_{22} L_e$  and the system (5) becomes

$$M_z = \overline{M_z} - MA_{22} L_e \ddot{f}. \quad (6)$$

As previously mentioned, inertial terms are negligible. As a result,  $I \ddot{\alpha}$  and  $M_{in}$  can be set to zero in (4). Using the quasi-static approach, this equation can be written as follows, with  $n + 1$  being the temporal iteration,  $k$  the previous iteration of the non-linear loop and  $k + 1$  the actual one:

$$K_{lin} f_{k+1}^{n+1} = M_z^{n+1}. \quad (7)$$

To make the writing clearer,  $n + 1$  is omitted as all quantities are expressed at the corresponding temporal iteration. We add to both sides of the last equation the added-mass term  $MA_{22} L_e \ddot{f}$ , at two different values of non-linear iteration to decrease the dependency of the right-hand side on the acceleration:

$$K_{lin} f_{k+1} + MA_{22} L_e \ddot{f}_{k+1} = M_z_k + MA_{22} L_e \ddot{f}_k. \quad (8)$$

This manipulation stabilizes the FSI coupling, by acting as a physical relaxation of the phenomenon (see equation (11)). It recovers the initial equation (7) at convergence. Since the BDF2 is used for the time integration, the increment of position  $\delta f_{k+1} = f_{k+1} - f_k$  is linked to the increment of acceleration  $\delta \ddot{f}_{k+1} = \ddot{f}_{k+1} - \ddot{f}_k$ . The link is a first-order approximation on the time step, expressed as follows:

$$\delta \ddot{f}_{k+1} = e_c^2 \delta f_{k+1}, \quad (9)$$

where  $e_c$  is a coefficient of BDF2 and its value is  $e_c = \frac{3}{2 \Delta t}$ , where  $\Delta t = t^{n+1} - t^n$ . Then, equation (8) can be rewritten as follows:

$$K_{lin} f_{k+1} + e_c^2 MA_{22} L_e f_{k+1} = M_z_k + e_c^2 MA_{22} L_e f_k. \quad (10)$$

Using the temporary value of  $f$ , denoted  $f_{imp}$  and obtained with the expression of the model (1) such as  $f_{imp} = M_z_k / K_{lin}$ , we can rewrite (10), after some manipulations, in a shorter way:

$$f_{k+1} = r f_{imp} + (1 - r) f_k, \quad (11)$$

with the relaxation coefficient  $r$  given by

$$r = \frac{1}{1 + \frac{e_c^2 MA_{22} L_e}{K_{lin}}}. \quad (12)$$

Using the model (10), the new value of the angular deflections is given by the relation

$$\alpha_{k+1} = \frac{K_{lin}}{K_{ang}} f_{k+1}. \quad (13)$$

For the first non-linear iteration (i.e. for  $k = 1$ ), of each temporal iteration, the values  $f_0$  and  $\alpha_0$  come from an extrapolation at the second order of the converged values at the two previous time steps.

### 2.3.4 Stabilisation using the added mass for the FSI coupling with the complete model

In the complete model,  $f$  and  $\alpha$  are independent. The system (2) that defines them in function of  $F_y$  and  $M_z$  can be written under a matrix form

$$\begin{pmatrix} f \\ \alpha \end{pmatrix}_{k+1} = B \begin{pmatrix} M_z \\ F_y \end{pmatrix}_k \quad \text{with} \quad B = \begin{pmatrix} a & b \\ c & d \end{pmatrix}, \quad (14)$$

and inversed, such as

$$B^{-1} \begin{pmatrix} f \\ \alpha \end{pmatrix}_{k+1} = \begin{pmatrix} M_z \\ F_y \end{pmatrix}_k, \quad (15)$$

with

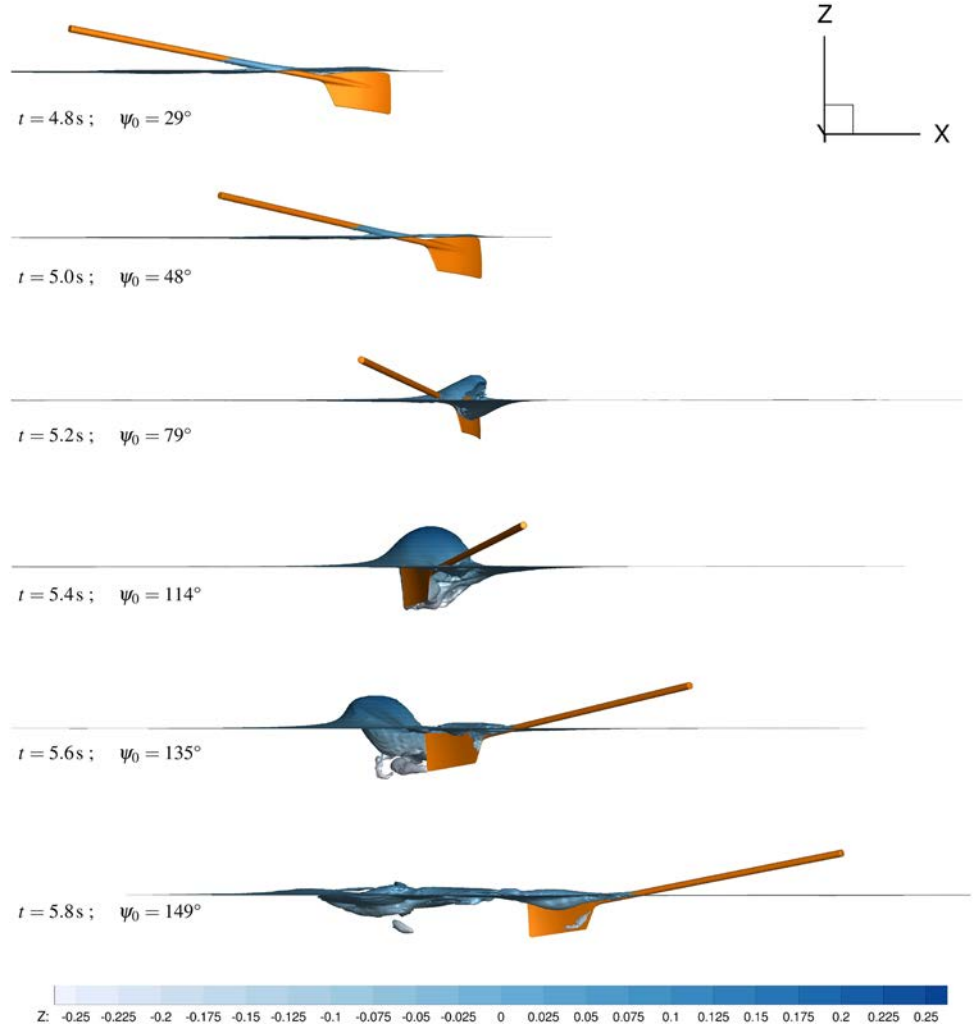
$$B^{-1} = \frac{1}{\Delta_B} \begin{pmatrix} d & -b \\ -c & a \end{pmatrix} \quad \text{and} \quad \Delta_B = \det(B) = a d - b c < 0. \quad (16)$$

We consider that the force  $F_y$  and the moment  $M_z$  depend on the diagonal term of the added-mass matrix and its corresponding DOF (respectively,  $\ddot{f}$  and  $\ddot{\alpha}$ ) and also on an extra-diagonal term associated to the other DOF (respectively,  $\ddot{\alpha}$  and  $\ddot{f}$ ). Therefore the expression (5) can be simplified under the form:

$$\begin{pmatrix} M_z \\ F_y \end{pmatrix} = \begin{pmatrix} \overline{M_z} \\ \overline{F_y} \end{pmatrix} - C \begin{pmatrix} \ddot{f} \\ \ddot{\alpha} \end{pmatrix}, \quad (17)$$

with

**Fig. 6** Visualisation, from a stationary location, looking in the hull-to-bank direction, of a simulation of a simplified rowing stroke. The free surface is coloured according to its vertical coordinate  $z$  (in m)



$$C = \begin{pmatrix} MA_{62} & MA_{66} \\ MA_{22} & MA_{26} \end{pmatrix}. \quad (18)$$

In a similar way than the simplified model, we add the added-mass terms on both sides of the matrix system (15) and we use the BDF2 to transform the increment of acceleration into an increment of position, through the  $e_c^2$  coefficient. This gives the following expression:

$$D \begin{pmatrix} f \\ \alpha \end{pmatrix}_{k+1} = \begin{pmatrix} M_z \\ F_y \end{pmatrix}_k + e_c^2 C \begin{pmatrix} f \\ \alpha \end{pmatrix}_k, \quad (19)$$

with

$$D = B^{-1} + e_c^2 C. \quad (20)$$

Finally, we can retrieve a more interesting expression with a left multiplication both sides by  $D^{-1}$ :

$$\begin{pmatrix} f \\ \alpha \end{pmatrix}_{k+1} = D^{-1} \begin{pmatrix} M_z \\ F_y \end{pmatrix}_k + e_c^2 D^{-1} C \begin{pmatrix} f \\ \alpha \end{pmatrix}_k. \quad (21)$$

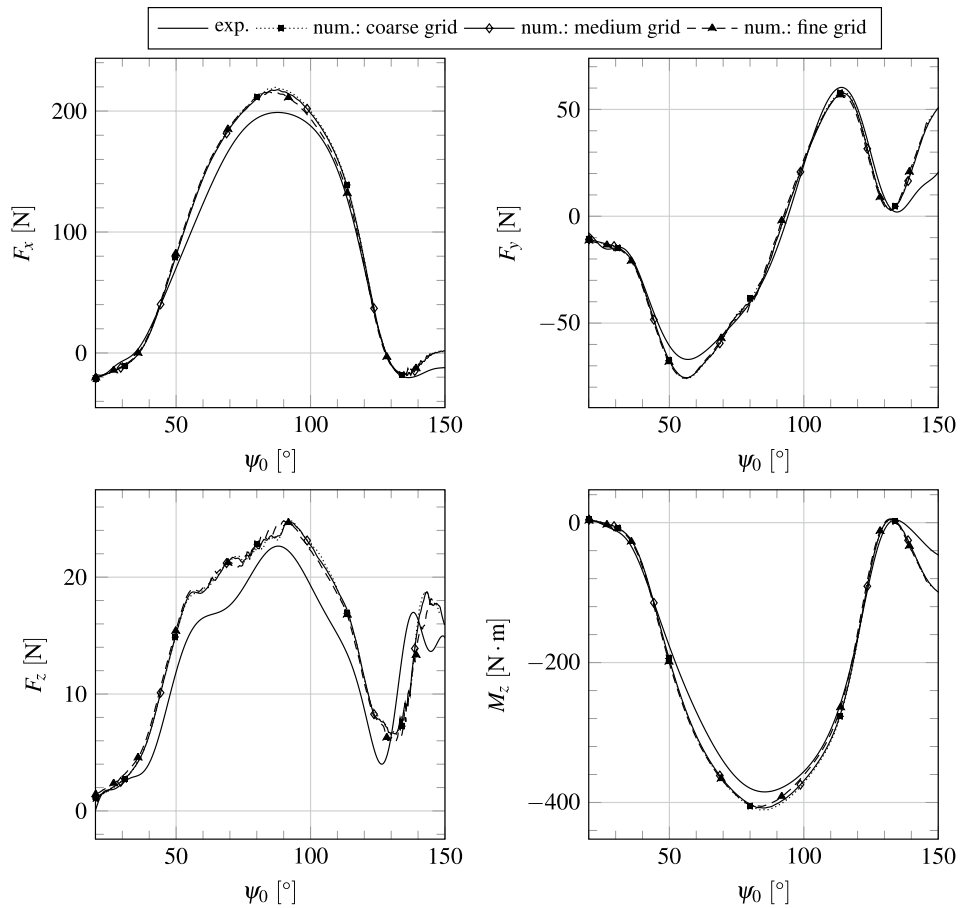
This expression is not developed because it would unnecessarily take space. It should be noted that, even with developments, a simple expression in the form of (11) cannot be found, where a relaxation coefficient would appear. Nevertheless the procedure acts similarly as a relaxation operator.

### 3 Results

Figure 6 shows six snapshots of the flow for the rowing stroke 154, obtained by a numerical simulation performed with a coarse grid of  $1.2 \cdot 10^6$  cells. The characteristics of a real rowing strokes are well reproduced. In particular, one can observe the breaking of the free surface and the creation of an air cavity behind the blade.

Two grid convergence studies were carried out with the three levels of mesh fineness of Table 2. They are based on two different experimental trials whose parameters are voluntarily chosen as different as possible in the available database: the smallest velocity against the largest simultaneously

**Fig. 7** Study of the grid convergence based on the angular evolution of the hydrodynamic forces  $F_x$ ,  $F_y$  and  $F_z$  and the moment  $M_z$  relative to the axis of rotation



with the largest immersion angle against the smallest (trials 67 and 154). As the results are similar, only the study of the trial 154 is presented. Figure 7 shows the evolutions of the hydrodynamic forces  $F_x$ ,  $F_y$  and  $F_z$  and the moment  $M_z$  relative to the axis of rotation, in function of the sweep angle  $\psi_0$ . The global shapes of the force curves of the experimental trials are well captured by the simulations. The propulsive force and moment have similar profiles and the same observations can be made. Numerical simulations overestimate from 5 to 12% the maxima. The error between experiments and simulations grows in the first half of the rowing stroke, till  $\psi_0 \approx 90^\circ$ , then it decreases up to  $\psi_0 \approx 130^\circ$  and it strongly increases until the end. The maxima of the force  $F_y$  are also overestimated, by the same order of magnitude. However, the profile is disturbed in the interval  $[70^\circ, 90^\circ]$ . Even if it is the least well fitted, the shape of the  $F_z$  profile is globally captured.

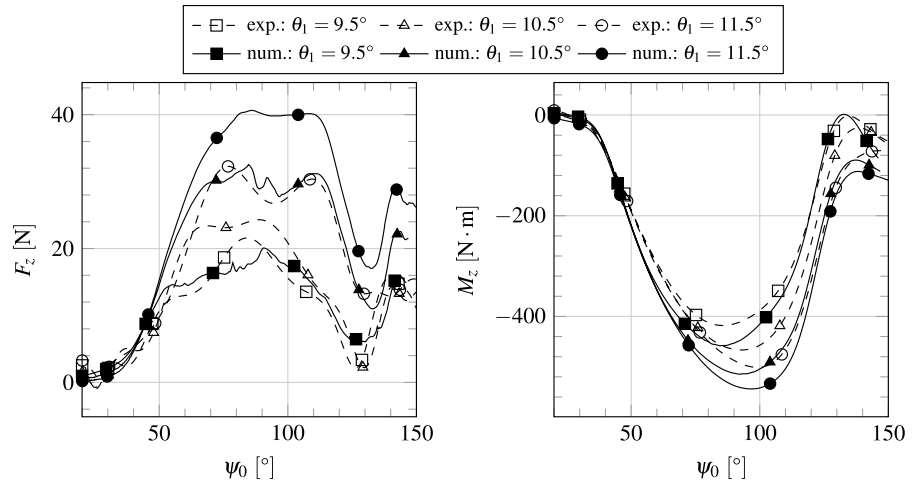
All the results obtained with the coarse, medium and fine meshes are really close, as visible in Fig. 7. The discretisation error of the coarse mesh is sufficiently limited and its maximal value occurs for  $\psi_0 \approx 90^\circ$  for the propulsive force  $F_x$  and moment  $M_z$ . For this particular angle, the decrease of the discretisation error between the coarse mesh and the fine mesh is only of about 2% (relatively to the experimental

value). So the coarse mesh is dense enough and has been chosen for the other computations later described. No study of time step convergence has been done because all simulations were carried out with a Courant number  $C_o < 0.3$  for the area surrounding the free surface, allowing the use the compressive property of the BRICS scheme in order to capture the free surface. The total CPU time needed for those computations is between about 1000 h (on 56 cores) for the coarse grids and 10000 h (on 224 cores) for the fine grids.

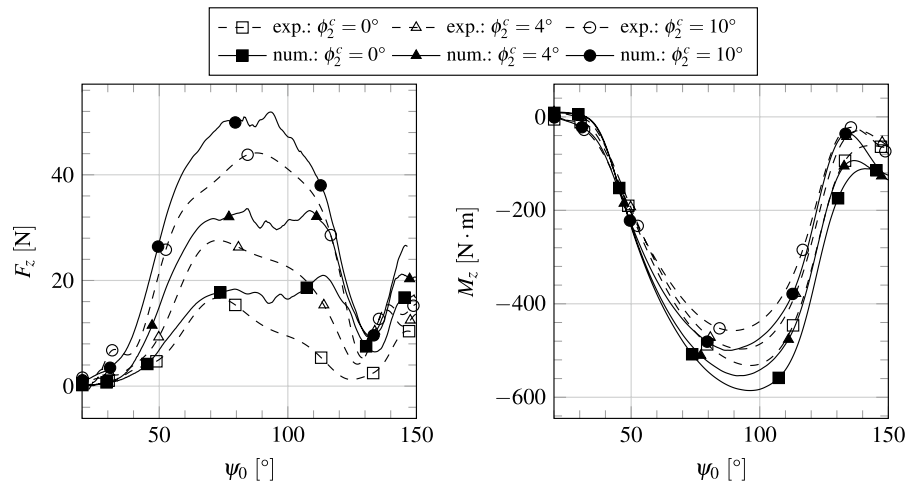
Using the quite rich database of results from the experimental campaign, two sets of rowing strokes were selected where only one parameter varies in each of them: the immersion and roll angles. The objective is to analyse the influence of those parameters and to check if the trends obtained experimentally are similar to those of the numerical simulations.

Figure 8 shows the influence of the immersion angle on the force  $F_z$  and moment  $M_z$ .  $F_z$  has been chosen rather than the propulsive force  $F_x$  or the transversal force  $F_y$  because these curves show similar trends compared to the one of  $M_z$ , so the comments would be identical. Curves of the same marker shape represent the same immersion angle. Those having filled markers associated with continuous lines are for the numerical signals and those with empty markers and

**Fig. 8** Influence of the immersion angle on the angular evolution of the hydrodynamic force  $F_z$  and moment  $M_z$



**Fig. 9** Influence of the roll angle on the angular evolution of the hydrodynamic force  $F_z$  and moment  $M_z$



dashed lines refer to the experiment data. Again, differences between experimental and numerical data are observed, especially for the low magnitude component  $F_z$  where the relative error is larger. However, the influence of  $\theta_1$  follows the same law in both cases: the maxima of the forces and moments are increasing functions of the immersion angle, for the tested values. With Fig. 9, the same remark can be drawn regarding the roll angle but only for the force  $F_z$ . The propulsive moment  $M_z$  has an opposite behaviour. Again the experimental trends are well captured by the simulations, even for the low magnitude vertical component of the force.

The influence of the models for the oar bending can be seen in Fig. 10, where the propulsive force  $F_x$  is plotted along the sweep angle for the simplified and the complete models. As expected the complete model gives a smaller error. At  $\psi_0 = 98^\circ$ , the error indeed decreases from 14 to 12%. Whatever the model, it clearly appears that the oar flexibility has a considerable effect on the propulsive force. When the oar is rigid, the force responds earlier in time

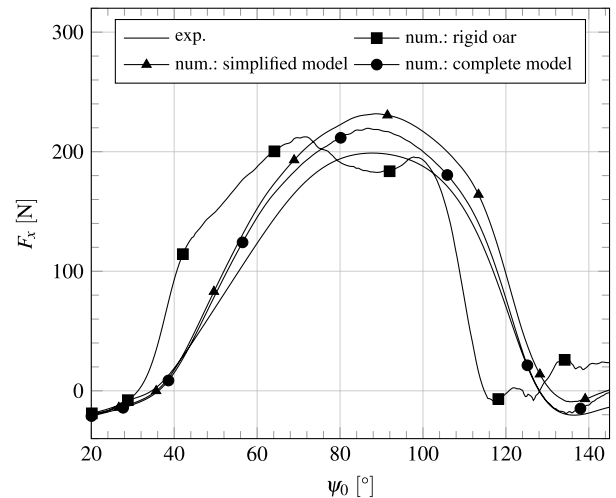


**Fig. 10** Influence of the model of oar bending on the angular evolution of the hydrodynamic force  $F_x$

(or in sweep angle) and undergoes more variations. The maximal values for the linear and angular deflections are, respectively, of about 12 cm and  $8^\circ$  for the simulation with the complete model. They are high enough to explain those different behaviours.

## 4 Discussion

The results for this configuration in laboratory are less error prone than those obtained in real conditions [15], because there are more uncertainties on the latter. In the first configuration the propulsive force and moment are overestimated by 5–12% while they are underestimated by 15–20% in the real situation. This margin of error is satisfactory given that the flow is highly unsteady with a violent free surface deformation. To the authors’ knowledge no other computations with this level of complexity have been published, making the comparison impossible. That is why we analyse the error in this discussion with a focus on its sources and its quantification.

### 4.1 Inventory of the possible sources of error

We propose a list of the main sources of error for both configurations: trials in laboratory and on site.

A first class of error is the experimental one. Unlike the in situ configuration where neither the roll of the boat nor the altitude of the blade were measured, here all the kinematics is known and available to be numerically reproduced. In addition to that, trials in laboratory benefits from a stable environment, which is not necessary the case of in situ measurements. However, even if uncertainties are more controlled in laboratory, they can affect the accuracy of derived quantities. Although the intrinsic error margins of each sensor is sufficiently small (lower than one percent) with a good enough repeatability, this can lead by propagation to higher uncertainties on some quantities of interest, as proved in 4.2. The accuracy and the repeatability of the measurements are here critical points due to the specific kinematic chain leading to the blade motion with respect to water. Regarding the in situ configuration, this issue is far more difficult to tackle since the velocity of the hull has large and abrupt variations. The velocity sensor itself and/or the associated low-pass filtering of its output signal may lead to a loss of frequential contents and a slight but still excessive smoothing. As a consequence, the reproduction of the real kinematics which is used to drive the simulation, especially the resulting acceleration may be altered and cause significant differences when comparing the fluid force, due to the fact that a large part of it depends on its acceleration with respect to water.

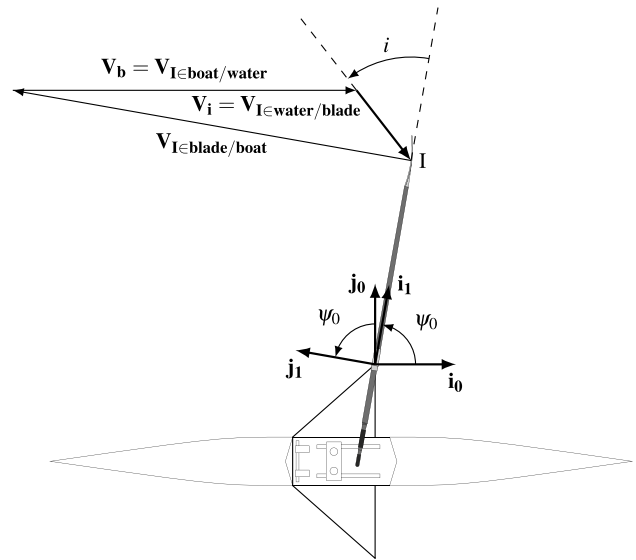


Fig. 11 Definition of the incident velocity on the oar blade

The numerical errors constitute a second class of error. First there is the modelling error, or the difference between the real flow and the mathematical model chosen to describe it. In this case the model for the resolution of the flow is made of the RANS equations, or the Euler model (null viscosity and slip condition on walls) for the real rowing stroke. Those models allow an accurate description of the physics, at least for the angular interval of interest (i.e. till the finish phase). However, those models fail at the end of this simplified stroke, i.e. for sweep angles such as  $\psi_0 > 130^\circ$ . Some additional investigations using more advanced turbulent models, such as DES (detached eddy simulation) or LES (large eddy simulation), could be useful, even if the cost would be high. Another modelling error should be examined, i.e. the boundary conditions. The effect of the vertical walls has been neglected but, as the blade comes near the lateral wall (about two chord lengths), it might be interesting to model the confinement effect. Then there is the discretisation error, that is to say the difference between the exact solution of the mathematical model and the one of the discretised equations implemented in the solver. Here we checked that the influence of the grid size is weaker than the observed difference with the experimental measurements. Finally, there is the convergence error, or the error between the exact solution of the discretised equations and the obtained solution after a finite number of iterations or when a given order of convergence is reached. In our computations, the convergence of the forces within each time step is checked a posteriori.

## 4.2 Study of the uncertainties on the forces

The hydrodynamic forces (or moments) applied on the blade depend on the incident velocity of the flow, which should be expressed at a point where the moment is null. As this characteristics cannot be always verified, one often chooses to express the velocity at an arbitrary point, approximately at the middle of the blade. In this study, this point is I (identical to E, see Fig. 11) and distant of  $L_I = 1.815$  m of the oarlock. For the sake of simplicity only one DOF is considered for the boat and one for the oar. Furthermore the flexibility of the oar is neglected. The boat moves at a constant velocity  $V_b = 4.202 \text{ m} \cdot \text{s}^{-1}$  along the  $(O, \mathbf{i}_0)$  axis. The oar rotates relative to the boat at the point B along the  $(B, \mathbf{k}_0)$  axis, at an angular velocity  $\dot{\psi}_0$  given by the law expressed in Fig. 3, and is inclined on the water of an angle  $\theta_1 = 9.5^\circ$ . So this configuration is similar to the trial 154.

The incident velocity  $\mathbf{V}_i$  of the flow relative to the blade is the opposite of the velocity of the point I belonging to the blade relatively to the water  $\mathbf{V}_{I \in \text{blade/water}}$  and is obtained by

$$\begin{aligned} \mathbf{V}_i &= -\mathbf{V}_{I \in \text{blade/water}} \\ &= -(\mathbf{V}_{I \in \text{blade/boat}} + \mathbf{V}_{I \in \text{boat/water}}), \end{aligned} \quad (22)$$

where  $\mathbf{V}_{I \in \text{boat/water}}$  is simply the velocity of the boat expressed in  $\mathfrak{R}_0$ ,  $\mathbf{V}_b = V_b \mathbf{i}_0$ , and  $\mathbf{V}_{I \in \text{blade/boat}} = L_I \cos \theta_1 \dot{\psi}_0 \mathbf{j}_1$  is expressed in the frame  $\mathfrak{R}_1$  associated to the oar (see Fig. 11). The incident velocity, expressed in  $\mathfrak{R}_1$ , is then equal to

$$\mathbf{V}_i = \begin{pmatrix} -V_b \cos \psi_0 \\ -L_I \cos \theta_1 \dot{\psi}_0 + V_b \sin \psi_0 \\ 0 \end{pmatrix}_{\mathfrak{R}_1}. \quad (23)$$

With a quantity  $\eta$  called kinematic efficiency (see Barré and Kobus [1]) and defined by

$$\eta = \frac{V_b \sin \psi_0}{L_I \cos \theta_1 \dot{\psi}_0}, \quad (24)$$

the norm of the incident velocity can be expressed by

$$V_i = V_b \sqrt{1 + \frac{1}{\eta} \left( \frac{1}{\eta} - 2 \right) \sin^2 \psi_0}, \quad (25)$$

and the incident angle, defined by the angle between  $\mathbf{i}_3$  (equivalent to  $\mathbf{i}_1$  and  $\mathbf{i}_2$  in this planar motion) and  $\mathbf{V}_i$  (see Fig. 11), is equal to

$$i = \arctan \left( \tan \psi_0 \left( \frac{1}{\eta} - 1 \right) \right). \quad (26)$$

Let  $\mathcal{Q}$  be a quantity depending on  $N$  parameters  $\mathcal{P}_k$ ,  $k \in \llbracket 1, N \rrbracket$ , each of them estimated with an absolute error  $\Delta \mathcal{P}_k$ ,  $\Delta \mathcal{P}_k > 0$ . The absolute error  $\Delta \mathcal{Q}$  on  $\mathcal{Q}$  can be estimated by the formula

$$\Delta \mathcal{Q} \leq \sum_{k=1}^N \left| \frac{\partial \mathcal{Q}}{\partial \mathcal{P}_k} \right| \Delta \mathcal{P}_k. \quad (27)$$

The parameters of  $V_i$  and  $i$  are  $\psi_0$ ,  $\dot{\psi}_0$ ,  $\theta_1$ ,  $V_b$  and  $L_I$ . To simplify the developments, we consider  $\psi_0$  and  $\dot{\psi}_0$  as independent. Moreover, we only select the parameters  $V_b$ ,  $\dot{\psi}_0$  and  $L_I$  for this study because a posteriori results show minor influences of  $\theta_1$  and  $\psi_0$  and it makes the formulation (28) shorter. We apply (27) for  $V_i$  and  $i$ . After some developments, the corresponding relative (for  $V_i$ ) and absolute (for  $i$ ) errors can be expressed as

$$\begin{aligned} \frac{\Delta V_i}{V_i} &\leq \left( \frac{V_b}{V_i} \right)^2 \left[ \left| 1 - \frac{\sin^2 \psi_0}{\eta} \right| \frac{\Delta V_b}{V_b} \right. \\ &\quad \left. + \frac{1}{\eta} \left| \frac{1}{\eta} - 1 \right| \sin^2 \psi_0 \left( \frac{\Delta L_I}{L_I} + \frac{\Delta \dot{\psi}_0}{\dot{\psi}_0} \right) \right] \end{aligned} \quad (28)$$

and

$$\Delta i \leq \frac{|\tan \psi_0|}{\eta(1 + \tan^2 i)} \left( \frac{\Delta V_b}{V_b} + \frac{\Delta L_I}{L_I} + \frac{\Delta \dot{\psi}_0}{\dot{\psi}_0} \right). \quad (29)$$

For  $\psi_0 = 90^\circ$ , we have  $i = 90^\circ$  and  $\Delta i = 0^\circ$  (see equations (26) and (29)). This means that the drag and propulsive forces are equal for this particular orientation. The quantification of the uncertainty on the propulsive force will only be given for this case because it is the more interesting one and a general approach would be more intricate. Using dimensional analysis,  $V_i$  (considered as constant for this specific case) and  $F_D$  are linked by

$$C_D = \frac{F_D}{\frac{1}{2} \rho A V_i^2}, \quad (30)$$

where  $\rho$  is the water density,  $A$  the projected area of the blade and  $C_D$  the drag coefficient. These three quantities are considered constant. As a result, the relative uncertainty on the propulsive force  $F_x$  follows the following inequality

$$\text{for } \psi_0 = 90^\circ, \quad \frac{\Delta F_x}{F_x} \leq 2 \frac{\Delta V_i}{V_i}. \quad (31)$$

As the goal is to quantify the uncertainties, values have to be given for the intrinsic uncertainties of the parameters. Since the real values are not known, we have chosen them in a quite fair manner. Indeed they are all three of about half a percent, which is supposed to give confidence for an

**Table 3** Parameters chosen for the uncertainty study, with their nominal values and their absolute and relative uncertainties

Parameter	Value	Absolute uncertainty	Relative uncertainty
$V_b$	$4.202 \text{ m} \cdot \text{s}^{-1}$	$2 \text{ cm} \cdot \text{s}^{-1}$	0.48%
$\psi_0$	$180.5 \text{ deg/s}^\dagger$	$1 \text{ deg/s}$	0.55% <sup>†</sup>
$L_I$	1.815 m	1 cm	0.55%

<sup>†</sup> For the maximum value of  $\psi_0$

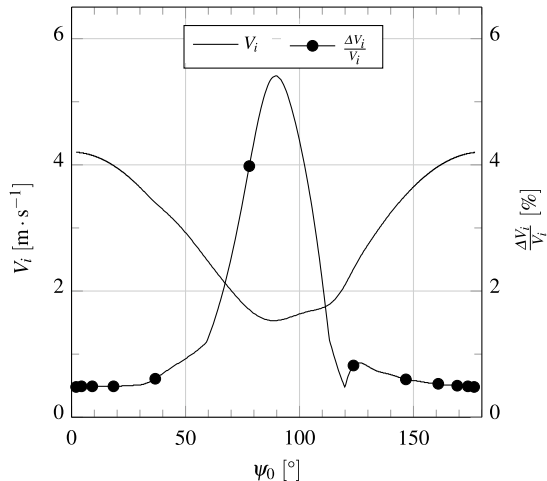


**Fig. 12** Evolution of the norm of the incident velocity  $V_i$  and its relative error  $\frac{\Delta V_i}{V_i}$  in function of the sweep angle  $\psi_0$

evaluation of the quantity of interest. The values are documented on Table 3. Using them we can plot the evolution of  $V_i$  and  $\frac{\Delta V_i}{V_i}$  relative to the sweep angle  $\psi_0$ , as done in Fig. 12.

$V_i$  is maximal and equal to  $V_b$  at both extremities of the stroke. Between them,  $V_i$  monotonically decreases, reaches its minimal value around  $\psi_0 \approx 90^\circ$  (i.e. when the propulsive force and moment are maximal) and increases till the end. The relative error has an inverted behaviour and it is therefore maximal when  $V_i$  is minimal. The corresponding value is of about 5.5%, indicating a relative error on the forces of 11%. This value is close to the gap obtained between the experimental and numerical results (i.e. 5–12%). In fact the uncertainty is higher because there should be an additional term on the right-hand side of (31), coming from the unsteady nature of  $C_D$  in this kind of flow which is not taken into account in equation (30). It demonstrates that our numerical simulations are robust enough and that the step of validation of our frame of modelling has been completed.

Figure 13 allows to understand the proportion of each parameter in the evolution of the relative error on  $V_i$  and likewise for the forces. The curves are plotted using the

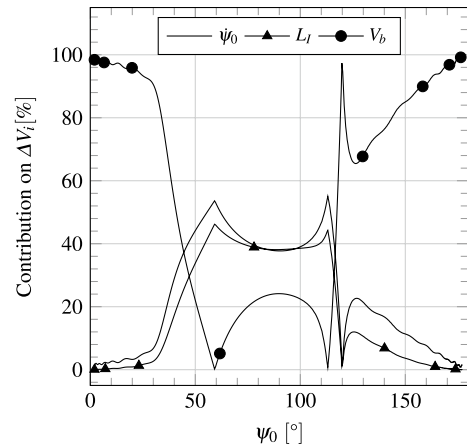


**Fig. 13** Evolution of the contributions of the parameters  $\psi_0$ ,  $L_I$  and  $V_b$  on the absolute error of the incident velocity in function of the sweep angle

right-hand side of the inequality (28). The parameter  $V_b$  has a dominant influence at both extremities of the stroke while  $L_I$  and  $\psi_0$  prevail more in the central part and behave similarly. The three parameters have equal influences for  $\psi_0 \approx 45^\circ$  and  $\psi_0 \approx 115^\circ$ . At  $\psi_0 = 90^\circ$ , where the propulsive force and moment are maximal, the parameters  $L_I$  and  $\psi_0$  account each for 38% of  $\Delta V_i$ , while  $V_b$  is responsible for 24% of this uncertainty. At  $\psi_0 = 59^\circ$  and  $\psi_0 = 113^\circ$ ,  $V_b$  has no influence on  $\Delta V_i$ . It is explained by the fact that  $\mathbf{V}_i$  is perpendicular to  $\mathbf{V}_b$  for those two orientations and, at the first order, a variation of  $V_b$  does not change  $V_i$  but only the angle  $i$ .

## 5 Conclusions

The frame of modelling and numerical simulation of a rowing stroke was tested and validated using an experimental database coming from trials performed in a towing-tank, whose measurements are less prone to uncertainties than those of experiments carried out in situ [15]. The counterpart of this configuration lies in the simplification of the rowing stroke, where two DOFs are lost for the propulsive phase: the rotation allowing the immersion of the oar on the water and the vertical translation. In addition the carriage of the towing tank moves at a constant velocity while a rowing boat has an unsteady kinematics.

In this more controlled configuration better results were obtained. The simulations are able to capture the profiles of the forces and to reproduce the trend induced by the variations of two parameters: the immersion and roll angles of the oar. They overestimate the maximum of the propulsive force  $F_x$  and moment  $M_z$  of 5–12% with the three levels of mesh fineness tested, meaning that the 1.2-million-cell mesh is

sufficient for those simulations. The errors between experimental and numerical results are close to the uncertainty of 11% obtained in a study with only three parameters whose intrinsic uncertainty were only of about 0.5% for each. On the one hand, this shows that the simulation framework is a robust tool for the simulation of a rowing stroke. On the other hand, the study of the uncertainties indicates that this kind of experiments is a very delicate task, even for a priori very controlled and stable environments.

A new model for the oar bending taking separately into account the hydrodynamic force and moment acting on the blade has been added to the existing procedure for the FSI coupling, allowing a more accurate evaluation of the linear and angular deflections. As these two DOFs are independent in this model, it may lead to oscillations followed by a divergence of the simulations. To avoid this situation, a method to stabilise the coupling has been developed, whose principle is to couple the relaxations of those variables including the off-diagonal terms of the added mass matrix.

The next step of this ongoing work is a co-simulation including the resolutions of both flows, the one around the blade and the one around the hull, and the resolution of the dynamics of the multibody boat–oars–rower system. The latter will be inspired of the work of Rongère et al. [17]. This frame will constitute the ambitious but necessary basis of a fine modelling for the analysis and the optimisation of the performance, like the influence of parameters.

**Acknowledgements** This work was granted access to the HPC resources of GENCI (Grand Equipement National de Calcul Intensif) under the allocation A0022A00129 and was supported by a grant from the Région Pays de la Loire through the project ANOPACY.

## References

- Barré S, Kobus JM (2010) Comparison between common models of forces on oar blades and forces measured by towing tank tests. *Proc Inst Mech Eng P J Sports Eng Technol* 224(1):37–50
- Caplan N, Gardner TN (2007) Optimization of oar blade design for improved performance in rowing. *J Sports Sci* 25(13):1471–1478
- Coppel AL, Gardner TN, Caplan N, Hargreaves DM (2010) Simulating the fluid dynamic behaviour of oar blades in competition rowing. *Proc Inst Mech Eng P J Sports Eng Technol* 224:25–35
- Hanna RK (2012) CFD in sport—a retrospective; 1992–2012. *Proc Eng* 34:622–627
- Henson VE, Meier Yang U (2002) BoomerAMG: a parallel algebraic multigrid solver and preconditioner. *Appl Numer Math* 41:155–177
- Kinoshita T, Miyashita M, Kobayashi H, Hino T (2008) Rowing velocity prediction program with estimating hydrodynamic load acting on an oar blade. In: Kato N, Kamimura S (eds) *Bio-mechanisms of swimming and flying*. Springer, Tokyo, pp 345–359
- Laschowski B, Hopkins CC, de Bruyn JR, Nolte V (2017) Modelling the deflection of rowing oar shafts. *Sports Biomech* 16(1):76–86
- Leroyer A, Barré S, Kobus JM, Visonneau M (2008) Experimental and numerical investigations of the flow around an oar blade. *J Mar Sci Technol* 13(1):1–15
- Leroyer A, Barré S, Kobus JM, Visonneau M (2010) Influence of free surface, unsteadiness and viscous effects on oar blade hydrodynamic loads. *J Sports Sci* 28(12):1287–1298
- Leroyer A, Barré S, Wackers J, Queutey P, Visonneau M, Kobus JM (2012) Validation of CFD simulations for unsteady violent free surface flows : the case of the hydrodynamics around rowing blades. In: 29th Symposium on Naval Hydrodynamics, Gothenburg, Sweden, 26-31 August 2012
- Leroyer A, Visonneau M (2005) Numerical methods for RANSE simulations of a self-propelled fish-like body. *J Fluids Struct* 20(7):975–991
- Menter FR (1993) Zonal two-equation  $k-\omega$  turbulence models for aerodynamic flows, 1993. *AIAA Pap* 96–2906:1–21
- Queutey P, Visonneau M (2007) An interface capturing method for free-surface hydrodynamic flows. *Comput Fluids* 36(9):1481–1510
- Robert Y (2017) Numerical simulation and modelling of tridimensional free-surface flows. Application to the boat-oars-rower system. Ph.D. thesis, Ecole Centrale de Nantes
- Robert Y, Leroyer A, Barré S, Rongère F, Queutey P, Visonneau M (2014) Fluid mechanics in rowing: the case of the flow around the blades., pp 744–749
- Robert Y, Leroyer A, Wackers J, Visonneau M, Queutey P (2015) Time-splitting procedure for the resolution of the volume fraction for unsteady flows. In: Bertram V, Campana EF (eds), 18<sup>th</sup> Numerical towing tank symposium. Cortona, Italy
- Rongère F, Khalil W, Kobus JM (2011) Dynamic modeling and simulation of rowing with a robotics formalism. In: 16th International conference on methods and models in automation and robotics (MMAR), 2011, pp 260–265
- Sliasis A, Tullis S (2009) The dynamic flow behaviour of an oar blade in motion using a hydrodynamics-based shell-velocity-coupled model of a rowing stroke. *Proc Institut Mech Eng P J Sports Eng Technol* 224:1–16
- Sliasis A, Tullis S (2009) Numerical modelling of rowing blade hydrodynamics. *Sports Eng* 12(1):31–40
- Sliasis A, Tullis S (2010) A hydrodynamics-based model of a rowing stroke simulating effects of drag and lift on oar blade efficiency for various cant angles. *Proc Eng* 2(2):2857–2862
- Söding H (2001) How to integrate free motions of solids in fluids. In: 4th Numerical towing tank symposium, Hamburg
- Videv TA, Doi Y (1993) Unsteady viscous flow simulation around the blade of rowing boat. *J Soc Naval Arch Jpn* 173:97–108
- Wackers J, Deng G, Leroyer A, Queutey P, Visonneau M (2012) Adaptive grid refinement for hydrodynamic flows. *Comput Fluids* 55(55):85–100
- Yvin C, Leroyer A, Visonneau M (2013) Co-simulation in fluid–structure interaction with rigid bodies. In: Numerical towing tank symposium 2013 (NuTTS’13)
- Yvin C, Leroyer A, Visonneau M, Queutey P (2018) Added mass evaluation with a finite-volume solver for applications in fluid–structure interaction problems solved with co-simulation. *J Fluids Struct* 81:528–546